

Structure and conductivity in the $\text{Bi}_4\text{Nb}_{1-x}\text{Y}_x\text{O}_{8.5-x}$ oxide-ion conducting system.

M. Holdynski,^{1,2*} M. Sinyureva,³ X. Liu,³ M. Leszczynska,¹ F. Krok,¹ S. Hull⁴ and I. Abrahams^{3*}

¹Faculty of Physics, Warsaw University of Technology, ul. Koszykowa 75, 00-662 Warsaw, Poland.

²Institute of Physical Chemistry, Polish Academy of Sciences, ul. Kasprzaka 44/52, 01-224 Warsaw, Poland.

³Materials Research Institute, School of Biological and Chemical Sciences, Queen Mary University of London, Mile End Road, London E1 4NS, U.K.

⁴The ISIS Facility, STFC Rutherford Appleton Laboratory, Didcot, Oxfordshire, OX11 0QX, U.K.

*Corresponding authors:

I. Abrahams e-mail: i.abrahams@qmul.ac.uk

M. Holdynski e-mail: mholdynski@ichf.edu.pl

Abstract

A study of structure and oxide-ion conductivity in the $\text{Bi}_4\text{Nb}_{1-x}\text{Y}_x\text{O}_{8.5-x}$ solid solution using X-ray and neutron powder diffraction and a.c. impedance spectroscopy is presented. Slow cooled samples are typically biphasic, exhibiting a mixture of cubic/pseudo-cubic and orthorhombic or tetragonal fluorite based phases. Single phase cubic and pseudo-cubic materials can be isolated by quenching from high temperatures. The defect structure in these quenched phases has been determined by neutron diffraction and shows an oxide-ion distribution that is compositionally dependent. This distribution is correlated with the compositional variation of the low temperature activation energy for total conductivity, whereas the activation energy for high temperature conductivity decreases with increasing value of x , reflecting the reduction in dopant-vacancy interaction with increasing yttrium content, as well as a change from a tetragonally ordered type III phase for low x -value compositions to a fully disordered $\delta\text{-Bi}_2\text{O}_3$ type phase at $x = 0.4$. Ordering phenomena are proposed to account for the appearance of a linear intermediate temperature region with high activation energy in Arrhenius plots of conductivity at $x \geq 0.4$. Conductivities in the order of $10^{-1} \text{ S cm}^{-1}$ are achieved at $700 \text{ }^\circ\text{C}$ in these materials.

Keywords:

Bismuth oxide, oxide-ion conductors; defect structure; neutron diffraction; X-ray diffraction; a.c. impedance spectroscopy.

1. Introduction

Many bismuth oxide based compounds are known to exhibit fast oxide-ion conduction. Indeed, the δ -phase of Bi_2O_3 itself shows the highest known oxide-ion conductivity in a solid, which is in the order of 1 S cm^{-1} at temperatures above $730 \text{ }^\circ\text{C}$ [1]. The high conductivity is attributed to a large oxide-ion vacancy concentration, as well as the polarizability of the cation framework. Although rapid quenching from high-temperature and low-temperature synthetic routes allow for isolation of δ - Bi_2O_3 at room temperature, this phase is in fact metastable at low temperatures. Low temperature “stabilisation” of δ -type phases can be achieved through solid-solution formation with other oxides and these have been extensively reviewed [2-8]. However, it has been argued that many of these phases are in fact metastable and prolonged annealing at intermediate temperatures (around $600 \text{ }^\circ\text{C}$) leads to ordering transitions to phases of lower symmetry [9].

The Bi_2O_3 - Nb_2O_5 binary system yields several ordered fluorite phases [10-14], which have been classified into four basic structural types (I to IV), with several subtypes [15,16]. The substitution of Nb^{5+} for Bi^{3+} leads to a reduction in the oxide-ion vacancy concentration, which is one of the reasons for lower ionic conductivity in these systems. Vacancy concentration can be increased through secondary subvalent doping of Nb^{5+} , for example by Y^{3+} [17], Zr^{4+} [18] or Er^{3+} [19]. The composition Bi_3NbO_7 has been well studied and has been shown to exhibit unusual polymorphism depending on thermal treatment [20-21]. At temperatures up to *ca.* $800 \text{ }^\circ\text{C}$, the incommensurately modulated type II phase is observed and can be considered as a pseudo-cubic phase, being closely related to the *fcc* fluorite structure [22]. In the range *ca.* 800 to $900 \text{ }^\circ\text{C}$ the type III phase is formed which shows a tetragonal distortion of the *fcc* lattice. Above $900 \text{ }^\circ\text{C}$ the pseudo-cubic phase reappears. Similar phase behaviour has been observed in $\text{Bi}_4\text{NbO}_{8.5}$ [23].

We have previously investigated the pseudo-binary systems Bi_3NbO_7 - Bi_3YO_6 [17] and $\text{Bi}_{3.5}\text{NbO}_{7.75}$ - $\text{Bi}_{3.5}\text{YO}_{6.75}$ [24], corresponding to Bi:M ratios of 3:1 and 3.5:1 respectively (where M = Nb and/or Y). Full solid solution ranges were observed in these systems based on a fluorite δ -phase type structure. As expected, the 3.5:1 system, being closer in composition to Bi_2O_3 , exhibited higher conductivities than those shown at the 3:1 Bi:M ratio. In both systems, oxide-ion distribution was seen to vary not only with composition, but also with temperature and was correlated with changes in the activation energy for conductivity.

Here we extend these studies to more bismuth rich compositions, with a Bi:M ratio of 4:1. As compositions become more bismuth rich, a variety of other phases can appear, the occurrence of which can be both compositionally and thermally dependent. Details of the structure-conductivity

relationship are studied through a combination of a.c. impedance spectroscopy and neutron and X-ray powder diffraction.

2. Experimental

2.1 Sample preparations

Compositions of general formula $\text{Bi}_4\text{Nb}_{1-x}\text{Y}_x\text{O}_{8.5-x}$ ($0.0 \leq x \leq 1.0$) were prepared by conventional solid-state synthesis. For neutron diffraction studies of large-scale samples (15 to 20 g), starting mixtures containing Bi_2O_3 (Aldrich, 99.9%), Nb_2O_5 (Aldrich, 99.9%) and Y_2O_3 (Aldrich, 99.99%) were ground as slurries in an agate mortar using industrial methylated spirits for 15 minutes. The dried mixtures were heated initially at 740 °C for 24 h, then cooled, reground and pelletised. Pellets were sintered at 800 °C for 10 h and either quenched in air or slow cooled in the furnace over a period of approximately 6 h.

For small-scale preparations and for preparation of pellets for impedance studies, identical starting mixtures were used, but ground in ethanol using a planetary ball mill. The dried mixtures were heated initially at 740 °C for 24 h, then cooled, reground in the ball mill and reheated at 800 °C for 24 h, before quenching to room temperature. The cooled samples were then further milled and pelletised. Pellets were pressed isostatically at a pressure of 400 MPa, and sintered at 900 °C for 10 h, before quenching in air to room temperature.

2.2 Electrical measurements

Electrical parameters were determined by a.c. impedance spectroscopy up to *ca.* 840 °C, using a fully automated Solartron 1255/1286 system, over the frequency range 1 Hz to 5×10^5 Hz. Samples for impedance measurements were prepared as rectangular blocks (*ca.* $6 \times 3 \times 3$ mm³) cut from quenched sintered pellets using a diamond saw. Platinum electrodes were sputtered by cathodic discharge on the two smallest faces. Impedance spectra were recorded over two cycles of heating and cooling at stabilised temperatures. Impedance at each frequency was measured repeatedly until consistency (2% tolerance in drift) was achieved or a maximum number of 25 repeats had been reached.

2.3 X-ray diffraction

X-ray powder diffraction data were collected on a Philips X'Pert Pro diffractometer fitted with an X'Celerator detector using Ni-filtered Cu-K α radiation in θ/θ geometry. The data were collected in the 2θ range 5-115° with a step width of 0.0167° and an effective count time of 300 s per step. Calibration was carried out with an external Si standard. Variable temperature X-ray

diffraction data were collected using an Anton-Paar HTK 1200 camera, with the room temperature scan parameters, at selected temperatures between 25 °C and 800 °C.

2.4 Neutron diffraction

Powder neutron diffraction data were collected on the Polaris diffractometer at the ISIS Facility, Rutherford Appleton Laboratory. Data collected on back-scattering and low-angle detectors over the time of flight ranges 1.0 to 20 and 0.5 to 20 ms were used in subsequent refinements. Samples were contained in cylindrical 11 mm diameter vanadium cans located in front of the back scattering detectors. Data sets of 200 μ A h were collected in each case.

2.5 Structure analysis

Structure refinement was carried out by Rietveld whole profile fitting using the program GSAS [25]. Where data were available from both X-ray and neutron diffraction measurements, combined refinements were carried out. Four basic structural models were used to analyse the data in this system (cubic, tetragonal, orthorhombic and rhombohedral) and where necessary a multiphase approach was used in refinement. Pseudo-cubic and cubic phases were modelled using a cubic cell of dimension $a \approx 5.56$ Å, in space group $Fm-3m$, as previously described [17]. Bi, Y and Nb were located on the ideal $4a$ site (0,0,0), with oxide-ions distributed over three sites; $8c$ at (0.25, 0.25, 0.25); $32f$ at approximately (0.3, 0.3, 0.3) and $48i$ at around (0.5, 0.2, 0.2), labelled O(1), O(2) and O(3), respectively. In the case of the $x = 0.2$ composition, a model based on the structure of $\text{Bi}_4\text{NbO}_{8.5}$ was used, with oxide-ions located on the $32f$ (0.3, 0.3, 0.3) and $24d$ (0.5, 0.25, 0.25) sites, labelled O(2) and O(3), respectively [23]. A total oxide-ion occupancy constraint was applied. Tetragonal phases were modelled using the structure proposed by Ling and Johnson [13] for the type III phase, in space group $I-4m2$, with approximate cell dimensions $a = 11.53$ Å and $c = 38.50$ Å. The rhombohedral phase, seen in the data for the $x = 1.0$ composition, was modelled on the structure of $\text{Bi}_{0.8}\text{Y}_{0.2}\text{O}_{1.5}$ presented by Zhang *et al.* [26], with approximate lattice parameters of $a = 4.02$ Å and $c = 27.59$ Å. The orthorhombic phase, which appeared as a secondary phase in slow cooled samples, was modelled using an orthorhombic subcell of approximate dimensions $a = 3.88$ Å, $b = 3.89$ Å and $c = 5.46$ Å, in space group $Immm$. The orthorhombic model was based on a simple distortion of the fluorite cell, such that $a_o \approx b_o \approx a_f\sqrt{2}$ and $c_o \approx c_f$ (where the subscripts o and f denote the orthorhombic and cubic fluorite cells respectively). Bi, Nb and Y atoms were located on the $2a$ site at 0, 0, 0 with O on the $4j$ site at *ca.* 0, 0.5, 0.25. Crystal and refinement parameters for the quenched samples are summarised in Table 1.

3. Results and Discussion

3.1 Phase behaviour in the $\text{Bi}_4\text{Nb}_{1-x}\text{Y}_x\text{O}_{8.5-x}$ system

Samples slow cooled from 800 °C exhibited diffraction patterns at room temperature that were clearly attributable to a fluorite lattice (Fig. 1). However, close inspection of some of these diffraction patterns revealed peak broadening, characteristic of low symmetry distortion and/or phase separation (Fig. 1 inset). These data were modelled using a multi-phase approach. For the $x = 0.0$ and $x = 0.2$ samples, a mixture of pseudo-cubic type II and tetragonal type III phases were found. For compositions $0.4 \leq x \leq 0.8$, the samples were predominantly cubic. However, peak broadening was clearly evident particularly in the $x = 0.4$ and $x = 0.6$ compositions. For $x = 1.0$, a pure cubic phase was observed.

In order to fit the diffraction data obtained for the $x = 0.4$ to $x = 0.8$ compositions, several models were tested including, cubic, tetragonal and orthorhombic distortions of the fluorite cell as well as mixtures of these phases. The most intense peak in the X-ray diffraction patterns at *ca.* 28.1° 2θ corresponds to the (111) reflection in cubic symmetry. The fact that this was observed to be split, ruled out a simple tetragonally distorted phase, but could correspond to either a mixture of cubic and orthorhombic phases or a mixture of cubic and tetragonal phases. The best fits were obtained for mixtures of orthorhombic and cubic phases. The orthorhombic model used was that of a subcell and did not take into account the observed superlattice peaks, since the orthorhombic polymorph appeared only as a secondary phase and therefore the intensity of these peaks was very weak. Fig. 2 shows a typical fit to the neutron diffraction data (data for the $x = 0.4$ sample are shown) for the mixed phase model. Since these samples were biphasic, further discussion of structure is limited to the monophasic quenched samples.

X-ray and neutron diffraction patterns for quenched samples in the $\text{Bi}_4\text{Nb}_{1-x}\text{Y}_x\text{O}_{8.5-x}$ ($0.4 \leq x \leq 1.0$) system at room temperature showed no evidence of the peak splitting seen in the slow-cooled samples. Only for the $x = 0.2$ composition, was there some evidence of a minor secondary phase in the neutron diffraction patterns (presumed to be the type III tetragonal phase). The fitted diffraction profiles for the $x = 0.2$ to $x = 1.0$ compositions are given in the supporting information as Figs. S1 to S5. At the lowest x -value composition, superlattice peaks are evident in the approximate d -spacing range 2.1 to 3.0 Å and around 5.0 Å. The peaks in the range 2.1 to 3.0 Å are replaced by a broad background feature associated with local ordering of defects at compositions above $x = 0.2$. The $x = 0.2$ composition exhibits the type II incommensurately modulated structure, recently described in detail by Ling *et al.* [22]. The incommensurate modulation is three dimensional and peaks in the diffraction pattern can be indexed using six indices (h, k, l, m, n, p) and a modulation parameter ε as:

$$\frac{1}{d_{hklmp}^2} = \frac{h^2 + k^2 + l^2 + \varepsilon(m^2 + n^2 + p^2)}{a^2} \quad (1)$$

In the case of the $x = 0.2$ composition, the value of ε is found to be 0.40(2) and compares with a value of 0.388 for $\text{Bi}_4\text{NbO}_{8.5}$ [23].

The compositional variation of the cubic unit cell parameter of quenched samples (Fig. 3) shows a general increase with increasing x -value, consistent with the expected increase in volume associated with substitution of Nb^{5+} by the larger Y^{3+} ion (with ionic radii of 0.64 Å and 0.900 Å, respectively for six-coordinate ions [27]). There is an apparent step in the plot at $x = 0.8$, with very similar lattice parameters for the $x = 0.8$ and 1.0 compositions. There are no significant differences in the diffraction patterns of the $x = 0.6$ and 0.8 compositions, other than a change in the lattice parameter. While, such a deviation from Vegard's law may result from local ordering, this must be interpreted cautiously since, if the $x = 0.8$ composition were ignored, Vegard's law appears to hold up to $x = 1.0$.

Variable temperature X-ray diffraction measurements were carried out on quenched samples to monitor the phase behaviour and lattice parameter variation. Detail of the X-ray diffraction patterns for the investigated compositions as a function of temperature are given in the supporting information as Figs. S6 to S10. For the $x = 0.2$ composition, peak broadening begins as early as 300 °C, with peak splitting clearly evident at 650 °C. There is some evidence of additional peaks at around 750 °C in the data for the $x = 0.4$ composition, but for the $x = 0.6$ and 0.8 compositions, a pure fluorite phase is seen throughout the temperature range studied. In the case of the $x = 1.0$ composition, additional peaks begin to appear at 550 °C and are clearly evident at 600 °C. These peaks are attributable to the rhombohedral phase previously described [9,28], associated with the well-known instability of the cubic phase at intermediate temperatures. At 700 °C a pure cubic phase is again observed, although it is noted that at 800 °C, weak additional peaks are again seen. Taking into account the second phase evident in the data for the slow cooled samples, the results confirm relatively poor stability of the cubic phase in this system.

Fig. 4 shows the thermal variation of cubic lattice parameter for the studied compositions in this system. The plots are fairly similar to each other and exhibit a degree of curvature. Each shows a linear low-temperature region up to around 400 °C and a linear high-temperature region from around 500 °C. Thus, the unit cell dimensions at high temperature are larger than would be expected from a simple thermal expansion of the lattice. We have previously discussed this

behaviour in related systems in terms of changes in the oxide-ion distribution and local vacancy ordering [29,30].

3.2 Defect structure of quenched phases

The refined structural parameters for the studied compositions in the $\text{Bi}_4\text{Nb}_{1-x}\text{Y}_x\text{O}_{8.5-x}$ system are given in Table 2. For the $x = 0.2$ composition, attempts to refine a model involving $8c$, $32f$ and $48i$ oxide-ion sites were unsuccessful and the previously described model for $\text{Bi}_4\text{NbO}_{8.5}$ [23], involving only $32f$ and $24d$ sites was used, giving a satisfactory fit (note no attempt was made to model the secondary type III phase here because of the weakness of the associated reflections). For all other compositions, oxide-ions were found to be distributed over three sites ($8c$, $32f$ and $48i$). There are subtle changes in the average structure with composition. In addition to the change in the O(3) position in shifting from the $24d$ to the $48i$ sites between $x = 0.2$ and 0.4 , there is a small but significant change in this position at $x = 0.8$. This results in longer M-O(3) distances and would be consistent with the larger than expected lattice parameter seen for this composition (Fig 4). The compositional variation of the oxide-ion site occupancies, presented as fractions of total oxide-ion content, is shown in Fig. 5. The most significant feature is the increase in the $8c$ fraction with increasing Y content, mainly at the expense of the $32f$ site fraction. At $x = 0.0$ there is no refineable fraction of $8c$ oxide-ions, while at $x = 1.0$ there are almost equal numbers of oxide-ions in the $8c$ and $32f$ sites. In order to interpret these results it is helpful to consider the locations of the $8c$ and $32f$ sites. Both lie within the tetrahedral cavity of the cubic close packed cation lattice. The $8c$ site represents the ideal centre of the site, while the $32f$ position is shifted towards the apices of the tetrahedral cavity. Thus, higher occupancy of the $32f$ site can be interpreted as greater disorder within the tetrahedral cavity. The $48i$ and $24d$ sites are close to each other and lie outside the tetrahedral cavity; these may be considered to be interstitial to the fluorite lattice. Oxide-ions on these sites allow the substituting cation to adopt more typical coordination environments. From Fig. 5 it is evident that after an initial small increase, the $48i/24d$ site fraction shows a small decrease with increasing x -value. These trends are similar to those seen in more heavily substituted bismuth yttrium niobates [17,24].

The variation of the Bi/Nb/Y-O (M-O) bond length in quenched samples is shown in Fig. 6. The M-O(1) distance increases slightly with increasing yttrium content, reflecting the small increase in cell volume. The M-O(2) distance decreases slightly with increasing Y content, while that of M-O(3) increases significantly to a maximum at $x = 0.8$. In $\delta\text{-Bi}_2\text{O}_3$, only the $32f$ and/or the $8c$ sites are found to be occupied [31-36]. This fact suggests, that in the present study, the $48i$ and $24d$ (O(3)) sites are exclusively associated with the dopant cations, Nb^{5+} and/or Y^{3+} . In addition, the fact that the $48i$ site occupancy changes little with the value of x , suggests that the association is to both Nb^{5+}

and Y^{3+} . The increase in the M-O(3) distance with increasing Y^{3+} content is consistent with this site becoming predominantly associated with Y^{3+} , as the smaller niobium cation is replaced by the larger yttrium cation.

From the refinements only an average picture of the cation coordination environment is obtained. The anion disorder makes interpretation of local structure difficult. Nevertheless, bearing in mind the short O-O distances that preclude simultaneous occupancy, the O:M ratios and the likely coordination geometries of the individual cations from their known crystal chemistry, it is possible to use the data in Table 2 to give probable coordination geometries for the individual cations in this system. As discussed above, oxide-ions on the 48*i* and 24*d* sites (O(3)) are likely to be mainly associated with the Y^{3+} and Nb^{5+} cations. The O(3):(Nb + Y) ratio decreases from 1.5 at $x = 0.2$ to 0.66 at $x = 0.8$ and 1.0 (Table 3). The increasing amount of oxide-ions on the O(1) site (8*c*) with increasing Y^{3+} content suggests that oxide-ions on this site are preferentially coordinated to Y^{3+} . The absence of occupation of the O(1) site in the Nb rich composition, $x = 0.2$ (and indeed $x = 0.0$ [23]) suggests Nb^{5+} is preferentially coordinated to ions on the O(2) site (32*f*). It is therefore possible to propose distorted octahedral geometries for Y^{3+} and Nb^{5+} based on these arguments (Fig. 7). In these models, six-coordinate geometry is completed by bonds to anions on the O(3) site. For these models a 1:1 ratio of O(3):(Nb + Y), as observed at $x = 0.4$ and 0.6, implies that since each substituent cation coordinates two shared O(3) oxide-ions and each ion on an O(3) site is shared between two cations, this would necessitate clustering of the substituent cations. Higher ratios would indicate less clustering of substituent polyhedra, while lower ratios suggest either lower coordination numbers for the substituent cations, or these cations adopting alternative coordination geometries with anions in the other sites.

The 8*c* and 32*f* sites are very close to each other and cannot be simultaneously occupied, the main difference being that oxide-ions on the ideal 8*c* site coordinate to four equidistant cations, whereas oxide-ions on the 32*f* site coordinate to only three. Similarly, oxide-ions on the 48*i* or 24*d* sites coordinate only two cations. Therefore, depending on the occupancies of these sites, the average cation coordination number can vary. For example, in δ - Bi_2O_3 the bismuth coordination number ranges from 4.5 for exclusive occupancy of the 32*f* sites to 6 for exclusive occupancy of the 8*c* sites [37]. The average cation coordination numbers are summarised in Table 3 and range from 4.68 for the $x = 0.2$ composition to 5.08 for the $x = 1.0$ composition. Assuming both the Y^{3+} and Nb^{5+} to be 6 coordinate, this leaves Bi^{3+} coordination numbers ranging from 4.35 to 4.86 for the $x = 0.2$ and 1.0 compositions, respectively. This suggests mixtures of 4 and 5 coordinated bismuth and is consistent with the known stereochemical activity of the Bi $6s^2$ lone pair. Proposed models for 4 and 5 coordinate bismuth atoms based on oxide-ions in the O(2) positions (32*f* sites) are shown in Fig. 7.

3.3 Electrical Conductivity

Representative impedance spectra are shown in Fig. 8. At lower temperatures a broadened high frequency semi-circle is seen with a blocking spike at lower frequencies attributable to the combined bulk and grain boundary response and the blocking electrode, respectively. It was not possible to reliably separate the bulk and grain boundary responses and hence all data reported here correspond to the total conductivity. At higher temperatures the bulk/grain boundary response moves out of the available frequency window and only the electrode response is observed. We have previously measured oxide-ion transference numbers in the closely related $\text{Bi}_{3.5}\text{Nb}_{1-x}\text{Y}_x\text{O}_{7.75-x}$ system [38]. This work showed that while in compositions with high niobium content there is some level of electronic conduction at lower temperatures, above 600 °C the system exhibits oxide-ion transference numbers close to unity. Even at low levels ($x = 0.2$) of substitution of Nb^{5+} by Y^{3+} , the electronic contribution to conductivity at low temperatures becomes negligible. In the more bismuth rich compositions in the present work, where the Nb^{5+} cations are more dilute, it is expected that ionic conductivity will predominate.

Fig. 9 shows the Arrhenius plots of total conductivity for samples of general composition $\text{Bi}_4\text{Nb}_{1-x}\text{Y}_x\text{O}_{8.5-x}$. For the $x = 0.0$ and $x = 0.2$ compositions two linear regions are seen, a low-temperature region extending to around 500 °C and a high-temperature region above this, with the high-temperature region possessing a higher activation energy than the low-temperature region. This change has previously been correlated with a change from the incommensurately ordered type II phase to the commensurately ordered tetragonal type III phase in the $x = 0.0$ composition [23]. Indeed, the variable temperature X-ray data for the $x = 0.2$ composition (Fig. S6) appear to confirm the partial appearance of the tetragonal phase at these temperatures. For compositions $x = 0.4$ to $x = 1.0$ the situation is somewhat different. In this compositional range three linear regions are observed, at low, intermediate and high temperatures. As for the lower x -value compositions, the initial change is to a linear region with higher activation energy, but occurs at a slightly lower temperature of around 450 °C. However, unlike the lower x -value compositions this region does not extend beyond *ca.* 550 °C, above which temperature a region with lower activation energy than both the intermediate and low temperature regions is observed. The low activation energy of the high-temperature region suggests that this region corresponds to the stability region of the fully disordered $\delta\text{-Bi}_2\text{O}_3$ type phase. This then begs the question as to what is the nature of the phase present in the intermediate-temperature region. The appearance of the intermediate-temperature region in the Arrhenius plots is correlated with the first appearance of occupancy of the $8c$ site (Fig. 5), suggesting some change in the oxide-ion/vacancy distribution. As with the lower x -value compositions, the higher activation energy of the intermediate-temperature region is likely to be

associated with ordering. However, apart from the $x = 1.0$ composition, where the rhombohedral phase occurs, there is no evidence for ordering or the appearance of other phases in the X-ray data and the cubic phase appears to be maintained throughout (Figs S7 to S10). This suggests that for these compositions ordering phenomena do not occur on the crystallographic scale. Indeed, changes in local ordering in both the cationic and anionic sublattices have been proposed to account for conductivity behaviour and conductivity decay in other δ -Bi₂O₃ based systems [39]. However, the fact that slow cooled samples do exhibit evidence for an orthorhombically ordered phase suggests that under certain conditions the ordering may extend to the long-range.

The values of conductivity at 300 °C, 500 °C and 700 °C (σ_{300} , σ_{500} and σ_{700} , respectively) are characteristic of the low, intermediate and high temperature regions. The compositional variation of these parameters is illustrated in Fig. 10. The plots for σ_{300} and σ_{700} are very similar to each other and show a general increasing trend with increasing x -value, as expected due to the increasing vacancy concentration. The plot for σ_{500} shows an initial decrease from $x = 0.0$ to $x = 0.2$ and then follows the trend of σ_{300} and σ_{700} plots. At these two compositions no separate linear region was seen at intermediate-temperatures in the Arrhenius plots. There is a local minimum at $x = 0.6$, the origin of which is unclear, but it does correspond to a region where the $32f$ and $8c$ oxygen site fractions level off (Fig. 5). The corresponding activation energies in the low, intermediate and high temperature regions (ΔE_{LT} , ΔE_{MT} and ΔE_{HT} respectively) are shown in Fig. 11 and reflect the variation of oxide-ion distribution shown in Fig. 5. The value for ΔE_{LT} shows a general increasing trend, associated with the increasing concentration of the less mobile $8c$ oxide-ions. At higher temperatures, where oxide-ion mobility is high, the values for ΔE_{HT} reflect not only the weakening of the dopant-vacancy interaction, as pentavalent Nb⁵⁺ is substituted by trivalent Y³⁺, but also the differences in the mobility of ions in the tetragonal type III phase at low x -values and the disordered δ -Bi₂O₃ type phase at $x = 0.4$ and above. As reflected in the Arrhenius plots, the values of ΔE_{MT} are all higher than the values at high and low temperatures. For compositions $x = 0.0$ and $x = 0.2$ the values are close to those for ΔE_{HT} , where the high and intermediate temperature regions are visually inseparable in the Arrhenius plots. From $x = 0.4$ to $x = 0.8$ there is little significant variation in ΔE_{MT} , with a significant increase seen between $x = 0.8$ and $x = 1.0$, correlated with the appearance of the rhombohedral phase in the X-ray data at these temperatures (Fig. S10).

4. Conclusions

A full solid solution range is obtained in the system Bi₄Nb_{1-x}Y_xO_{8.5-x} ($0.0 \leq x \leq 1.0$). Compositions containing both niobium and yttrium are difficult to prepare as single phases, exhibiting both cubic and orthorhombic or tetragonal polymorphs in slow cooled samples. Single

phase materials can be obtained by quenching from high temperatures and show a cubic or pseudo-cubic fluorite type structure. The oxide-ion distribution in the quenched phases was seen to be compositionally dependent, with increasing yttrium content favouring the ideal $8c$ site in preference to the $32f$ site. Ions in the interstitial $48i$ or $24d$ sites allow for octahedral geometry to be adopted by the substituent cations, with some evidence of substituent cation clustering in this system. Average Bi coordination numbers vary between 4.35 to 4.85, consistent with stereochemical activity of the Bi $6s^2$ lone pair.

Conductivity is generally seen to increase with increasing vacancy concentration as pentavalent niobium is replaced by trivalent yttrium. The system shows appreciable levels of conductivity in the order of 10^{-1} S cm^{-1} at 700 °C. The compositional variation of activation energy for total conductivity at low temperatures is seen to be correlated with compositional changes in the oxide-ion distribution, while for compositions with $x \geq 0.4$ higher activation energies at intermediate temperatures appear to be associated with ordering phenomena. The high temperature activation energy shows a general decrease with decreasing dopant-vacancy interaction.

Acknowledgements

We are grateful to the STFC ISIS facility, Rutherford Appleton Laboratory, UK for beam time and to Dr Ron Smith for his help in data collection.

References

1. T. Takahashi, H. Iwahara, Y. Nagaj, *J. Appl. Electrochem.*, 2 (1972) 97.
2. G. Mairesse, in *Fast Ion Transport in Solids*, B. Scrosati, A. Magistris, C.M. Mari, G. Mariotto (Eds.), Kluwer Academic Publishers, Dordrecht, 1993, p271.
4. J.C. Boivin, G. Mairesse, *Chem. Mater.*, 10 (1998) 2870.
5. P. Shuk, H.D. Wiemhöfer, U. Guth, W. Göpel, M. Greenblatt, *Solid State Ionics*, 89 (1996) 179.
6. A.M. Azad, S. Larose, S.A. Akbar, *J. Mater. Sci.*, 29 (1994) 4135.
7. N.M. Sammes, G.A. Tompsett, H. Näfe, F. Aldinger, *J. Eur. Ceram. Soc.*, 19 (1999)1801.
8. M. Drache, P. Roussel, J-P Wignacourt, *Chem. Rev.*, 107 (2007) 80.
9. A. Watanabe, *Solid State Ionics*, 40/41 (1990) 889.
10. W. Zhou, D.A. Jefferson, J.M. Thomas, *Proc. R. Soc. Lond. A*, 406 (1986) 173.
11. C.D. Ling, R.L. Withers, S. Schmid, J.G. Thompson, *J. Solid State Chem.*, 137 (1998) 42.
12. A. Castro, E. Aguado, J.M. Rojo, P. Herrero, R. Enjalbert, J. Galy, *Mater. Res. Bull.*, 33 (1998) 31.
13. C.D. Ling, M. Johnson, *J. Solid State Chem.*, 177 (2004) 1838.
14. R.L. Withers, C.D. Ling, S. Schmid, *Z. Kristallogr.* 214 (1999) 296.

15. W. Zhou, *J. Solid State Chem.*, 101 (1992) 1.
16. C.D. Ling, *J. Solid State Chem.*, 148 (1999) 380.
17. I. Abrahams, A. Kozanecka-Szmigiel, F. Krok, W. Wrobel, S.C.M. Chan, and J.R. Dygas, *Solid State Ionics*, 177 (2006) 1761.
18. F. Krok, I. Abrahams, W. Wrobel, S.C.M. Chan, A. Kozanecka, T. Ossowski, *Solid State Ionics*, 175 (2004) 335.
19. M. Leszczynska, M. Holdynski, F. Krok, I. Abrahams, X. Liu and W. Wrobel, *Solid State Ionics*, 181 (2010) 796-811.
20. M. Valant, D. Suvorov, *J. Am. Ceram. Soc.*, 86 (2003) 939.
21. X.P. Wang, G. Corbel, S. Kodjikian, Q.F. Fang, P. Lacorre, *J. Solid State Chem.*, 179 (2006) 3338.
22. C. D. Ling, S. Schmid, P. E. R. Blanchard, V. Petříček, G. J. McIntyre, N. Sharma, A. Maljuk, A. A. Yaremchenko, V. V. Kharton, M. Gutmann, R. L. Withers, *J. Am. Chem. Soc.*, 135 (2013) 6477.
23. M. Holdynski, M. Sinyureva, X. Liu, W. Wrobel, J.R. Dygas, M. Pisarek, R.M. Nix, F. Krok, I. Abrahams, *J. Phys.: Condens. Matter*, 24 (2012) 045904.
24. F. Krok, I. Abrahams, M. Holdynski, A. Kozanecka-Szmigiel, M. Malys, M. Struzik, X. Liu and J.R. Dygas, *Solid State Ionics*, 179 (2008) 975-980.
25. A. C. Larson, R. B. Von Dreele, *Los Alamos National Laboratory Report*, No. LAUR-86-748, (1987).
26. X.-J. Zhang, W.-T.; Jin, S.-J. Hao, Y. Zhao, H. Zhang, *J. Supercond. Nov. Magn.*, 23 (2010) 23, 1011.
27. R.D. Shannon *Acta Crystallogr.*, A32 (1976) 751.
28. A. Watanabe, *Solid State Ionics* 86-88 (1996) 1427.
29. X. Liu, I. Abrahams, S. Hull, S.T. Norberg, M. Holdynski and F. Krok, *Solid State Ionics*, 192 (2011) 176-180.
30. I. Abrahams, X. Liu, S. Hull, S.T. Norberg, F. Krok, A. Kozanecka-Szmigiel, M. S. Islam, S.J. Stokes, *Chem. Mater.*, 22 (2010) 4435-3345.
31. P.D. Battle, C.R.A. Catlow, J. Drennan, A.D. Murray, *J. Phys C*, 16 (1983) 561.
32. S. Hull, S. T. Norberg, M. G. Tucker, S. G. Eriksson, C. E. Mohn, S. Stølen, *Dalton Trans.* (2009), 8737-8745.
33. G. Gattow and H. Schroeder, *Z. Anorg. Allgem. Chem.*, 318 (1962) 176
34. F. Hund, *Z. Anorg. Allgem. Chem.*, 333 (1964) 248.
35. H.A. Harwig, *Z. Anorg. Allgem. Chem.*, 444 (1978) 151.
36. M. Yashima and D. Ishimura, *Chem. Phys. Lett.*, 378 (2003) 395.

37. I. Abrahams, F. Krok, S.C.M. Chan, W. Wrobel, A. Kozanecka-Szmigiel, A. Luma, and J.R. Dygas, *J. Solid State Electrochem.*, 10 (2006) 569.
38. M. Malys, M. Holdynski, F. Krok, W. Wrobel, J.R.Dygas, C.Pirovano, R-N. Vannier, E. Capoen and I.Abrahams *J. Power Sources*, 194 (2009) 16.
39. K.Z. Fung, H.D. Baek, A. Virkar, *Solid State Ionics* 52 (1992) 199.

Table 1

Crystal and refinement parameters for for quenched samples of $\text{Bi}_4\text{Nb}_{1-x}\text{Y}_x\text{O}_{8.5-x}$ ($0.2 \leq x \leq 1.0$) at 25 °C.^a Estimated standard deviations are given in parentheses.

x		0.2	0.4	0.6	0.8	1.0
Formula		$\text{Bi}_{0.8}\text{Nb}_{0.16}\text{Y}_{0.04}\text{O}_{1.66}$	$\text{Bi}_{0.8}\text{Nb}_{0.12}\text{Y}_{0.08}\text{O}_{1.62}$	$\text{Bi}_{0.8}\text{Nb}_{0.08}\text{Y}_{0.12}\text{O}_{1.58}$	$\text{Bi}_{0.8}\text{Nb}_{0.04}\text{Y}_{0.16}\text{O}_{1.54}$	$\text{Bi}_{0.8}\text{Y}_{0.2}\text{O}_{1.5}$
M_r (g mol ⁻¹)		212.16	211.36	210.56	209.76	208.96
Crystal system		Cubic	Cubic	Cubic	Cubic	Cubic
Space Group		$Fm\bar{3}m$	$Fm\bar{3}m$	$Fm\bar{3}m$	$Fm\bar{3}m$	$Fm\bar{3}m$
a (Å)		5.49251(4)	5.49690(3)	5.50083(3)	5.50907(4)	5.51047(4)
Volume (Å ³)		165.696(3)	166.094(3)	166.450(3)	167.199(3)	167.327(3)
Z		4	4	4	4	4
ρ_{calc} (g cm ⁻³)		8.507	8.453	8.403	8.333	8.295
R-factors Neut. BS	R_{wp}	0.0174	0.0131	0.0117	0.0108	0.0094
	R_{p}	0.0256	0.0198	0.0180	0.0170	0.0163
	R_{ex}	0.0063	0.0071	0.0063	0.0069	0.072
	R_{F}^2	0.0685	0.0450	0.1012	0.0712	0.0924
R-factors Neut. LA	R_{wp}	0.0299	0.0255	0.0242	0.0213	0.0223
	R_{p}	0.0251	0.0227	0.0212	0.0204	0.0208
	R_{ex}	0.0224	0.0233	0.0207	0.0245	0.0237
	R_{F}^2	0.0677	0.0742	0.0985	0.0907	0.1156
R-factors X-ray	R_{wp}	0.0335	0.0327	0.271	0.0252	0.0329
	R_{p}	0.0192	0.0182	0.0142	0.0131	0.0196
	R_{ex}	0.0117	0.0117	0.0091	0.0097	0.0089
	R_{F}^2	0.0455	0.0546	0.0609	0.0834	0.0683
R-factors Overall	R_{wp}	0.0249	0.0234	0.0209	0.0194	0.0252
	R_{p}	0.0192	0.0182	0.0142	0.0134	0.0196
χ^2		6.207	4.819	5.377	3.962	7.016
No. of variables		130	132	132	130	108
No. of points	Neut. BS	3361	3362	3362	3362	3362
	Neut. LA	4243	4243	4243	4243	4243
	X-ray	6582	6582	6582	6582	6582
No. of refl.	Neut. BS	50	48	46	48	43
	Neut. LA	33	33	31	31	29
	X-ray	30	30	30	30	30

^a Neut. BS and Neut. LA refer to backscattering and low angle data neutron data, respectively. A definition of R-factors is given in reference 25.

Table 2
Refined atomic parameters and significant contact distances (Å) for
for quenched samples of $\text{Bi}_4\text{Nb}_{1-x}\text{Y}_x\text{O}_{8.5-x}$ ($0.2 \leq x \leq 1.0$) at 25 °C.

Estimated standard deviations are given in parentheses.

x	0.2	0.4	0.6	0.8	1.0	
Bi/Nb/Y site	$4a$	$4a$	$4a$	$4a$	$4a$	
Bi/Nb/Y x, y, z	0.0	0.0	0.0	0.0	0.0	
Bi/Nb/Y Occ.	0.8/0.16/0.04	0.8/0.12/0.08	0.8/0.08/0.12	0.8/0.04/0.16	0.8/0.0/0.2	
Bi/Nb/Y U_{iso} (Å ²)	0.0271(2)	0.0287(2)	0.0335(1)	0.0345(2)	0.0465(5)	
O(1/2/3/4) U_{iso} (Å ²)	0.0631(11)	0.0649(10)	0.0669(9)	0.0622(12)	0.0686(13)	
O(1)	site		$8c$	$8c$	$8c$	
	x, y, z		0.25	0.25	0.25	
	occ.		0.086(19)	0.249(13)	0.261(16)	0.356(12)
O(2)	site	$32f$	$32f$	$32f$	$32f$	
	x, y, z	0.2906(3)	0.2936(9)	0.3011(9)	0.3026(12)	0.3098(14)
	occ.	0.170(1)	0.155(5)	0.112(3)	0.112(4)	0.082(3)
O(3)	site	$24d$	$48i$	$48i$	$48i$	
	x	0.5	0.5	0.5	0.5	
	y, z	0.25	0.2104(19)	0.1908(17)	0.1664(32)	0.1982(34)
	occ.	0.050(1)	0.017(1)	0.016(1)	0.011(1)	0.011(1)
Bi/Nb/Y–O(1)		2.38023(1)	2.38193(1)	2.38550(1)	2.38610(1)	
Bi/Nb/Y–O(2)	2.2789(4)	2.276(1)	2.267(1)	2.269(2)	2.261(1)	
Bi/Nb/Y...O(2)'	2.764(3)	2.795(8)	2.869(9)	2.878(12)	2.957(13)	
Bi/Nb/Y–O(3)	1.94189(1)	1.968(2)	1.999(3)	2.054(8)	1.990(5)	

Table 3

Selected oxide-ion to cation ratios, average cation coordination number (\overline{CN}_M) and average bismuth coordination number (\overline{CN}_{Bi}) for quenched samples of $Bi_4Nb_{1-x}Y_xO_{8.5-x}$ ($0.2 \leq x \leq 1.0$) at 25 °C. Calculations are based on the assumption of six-coordinate geometry for Nb^{5+} and Y^{3+} cations.

x	O1:M	O2:M	O3:M	O3:(Y+Nb)	\overline{CN}_M	\overline{CN}_{Bi}
0.2	0.00	1.36	0.30	1.50	4.68	4.35
0.4	0.17	1.24	0.21	1.03	4.82	4.53
0.6	0.50	0.90	0.19	0.96	5.06	4.83
0.8	0.52	0.90	0.13	0.66	5.04	4.80
1.0	0.71	0.66	0.13	0.66	5.08	4.85

Figure Captions

Fig. 1. Neutron diffraction patterns (back scattering data) for slow cooled samples of composition $\text{Bi}_4\text{Nb}_{1-x}\text{Y}_x\text{O}_{8.5-x}$. Inset shows detail of (2 2 0) peak showing secondary phase with low symmetry distortion.

Fig. 2. Typical fit to the neutron diffraction data for a slow cooled sample of $\text{Bi}_4\text{Nb}_{1-x}\text{Y}_x\text{O}_{8.5-x}$ (back scattering data for the $x = 0.4$ sample are shown) using a mixed phase model. Observed (+ symbols), calculated (line) and difference (lower) profiles are shown. Reflection positions for the cubic (lower) and orthorhombic (upper) phases are indicated by markers.

Fig. 3. Compositional variation of the cubic unit cell parameter, a , in samples of composition $\text{Bi}_4\text{Nb}_{1-x}\text{Y}_x\text{O}_{8.5-x}$ quenched from high temperature. Data for the $x = 0.0$ composition are from [23].

Fig. 4. Thermal variation of the cubic unit cell parameter, a , in samples of composition $\text{Bi}_4\text{Nb}_{1-x}\text{Y}_x\text{O}_{8.5-x}$ quenched from high temperature. Data for the $x = 0.0$ composition are from [23].

Fig. 5. Compositional variation of oxide-ion site occupancies in samples of $\text{Bi}_4\text{Nb}_{1-x}\text{Y}_x\text{O}_{8.5-x}$ quenched from high temperature. Values are presented as fraction of total oxide-ion content. Data for the $x = 0.0$ composition are from [23].

Fig. 6. Compositional variation in M-O bond lengths in samples of $\text{Bi}_4\text{Nb}_{1-x}\text{Y}_x\text{O}_{8.5-x}$ quenched from high temperature. (M = Bi/Nb/Y).

Fig. 7. Proposed coordination geometries for (a) Nb, (b) Y, (c) 4-coordinate Bi and (d) 5-coordinate Bi in quenched samples of $\text{Bi}_4\text{Nb}_{1-x}\text{Y}_x\text{O}_{8.5-x}$. Images were generated from the refined structural parameters for the $x = 0.4$ composition.

Fig. 8. Representative impedance spectra at (a) 300 °C, (b) 500 °C and (c) 700 °C. Data for the $x = 0.4$ composition are shown.

Fig. 9. Arrhenius plots of total conductivity for compositions in the $\text{Bi}_4\text{Nb}_{1-x}\text{Y}_x\text{O}_{8.5-x}$ system. Data for the $x = 0.0$ composition are from [23].

Fig. 10. Compositional variation of low temperature (σ_{300}), intermediate temperature (σ_{500}), and high temperature (σ_{700}) conductivity in the $\text{Bi}_4\text{Nb}_{1-x}\text{Y}_x\text{O}_{8.5-x}$ system. Data for the $x = 0.0$ composition are from [23].

Fig. 11. Compositional variation of low-temperature (ΔE_{LT}), intermediate-temperature (ΔE_{MT}) and high-temperature (ΔE_{HT}) activation energies. Data for the $x = 0.0$ composition are from [23].

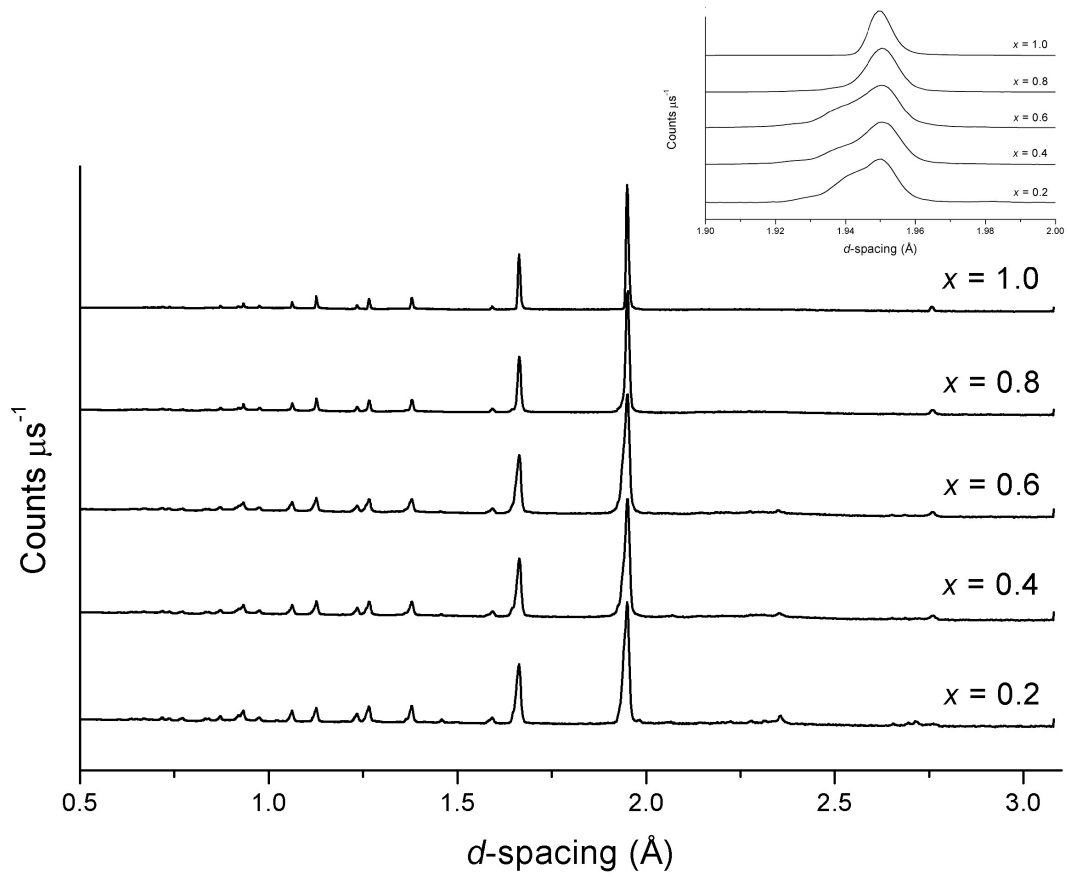


Fig. 1. Neutron diffraction patterns (back scattering data) for slow cooled samples of composition $\text{Bi}_4\text{Nb}_{1-x}\text{Y}_x\text{O}_{8.5-x}$. Inset shows detail of $(2\ 2\ 0)$ peak showing secondary phase with low symmetry distortion.

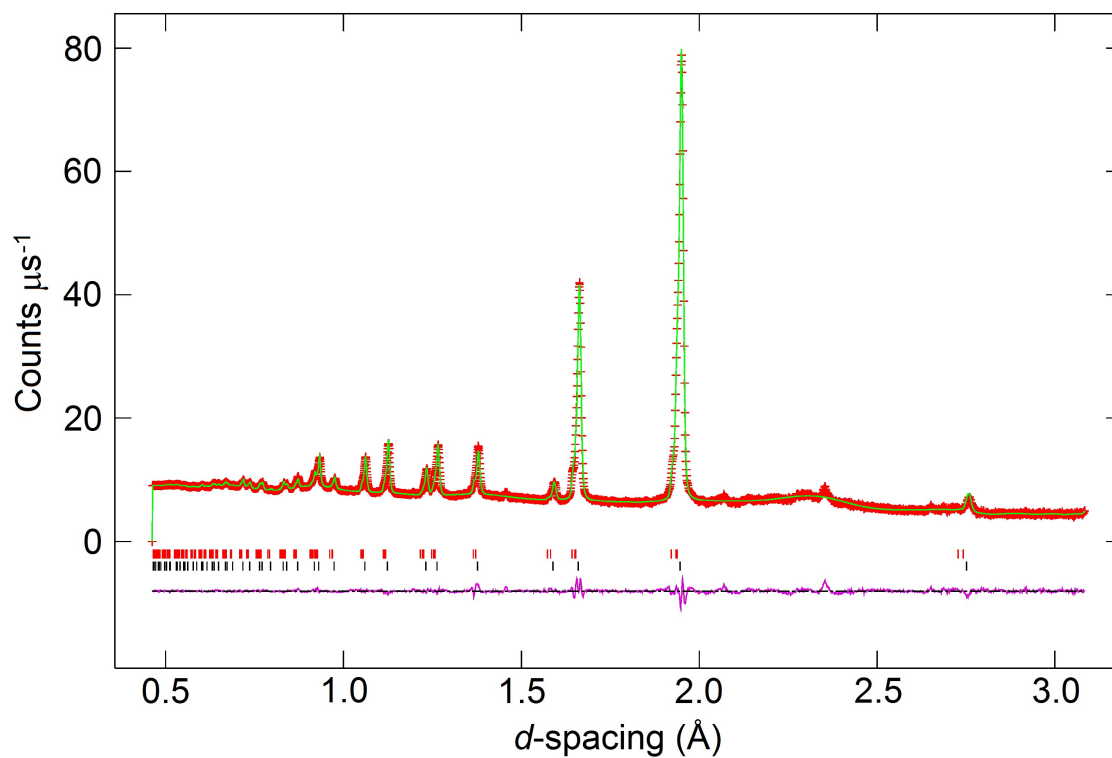


Fig. 2. Typical fit to the neutron diffraction data for a slow cooled sample of $\text{Bi}_4\text{Nb}_{1-x}\text{Y}_x\text{O}_{8.5-x}$ (back scattering data for the $x = 0.4$ sample are shown) using a mixed phase model. Observed (+ symbols), calculated (line) and difference (lower) profiles are shown. Reflection positions for the cubic (lower) and orthorhombic (upper) phases are indicated by markers.

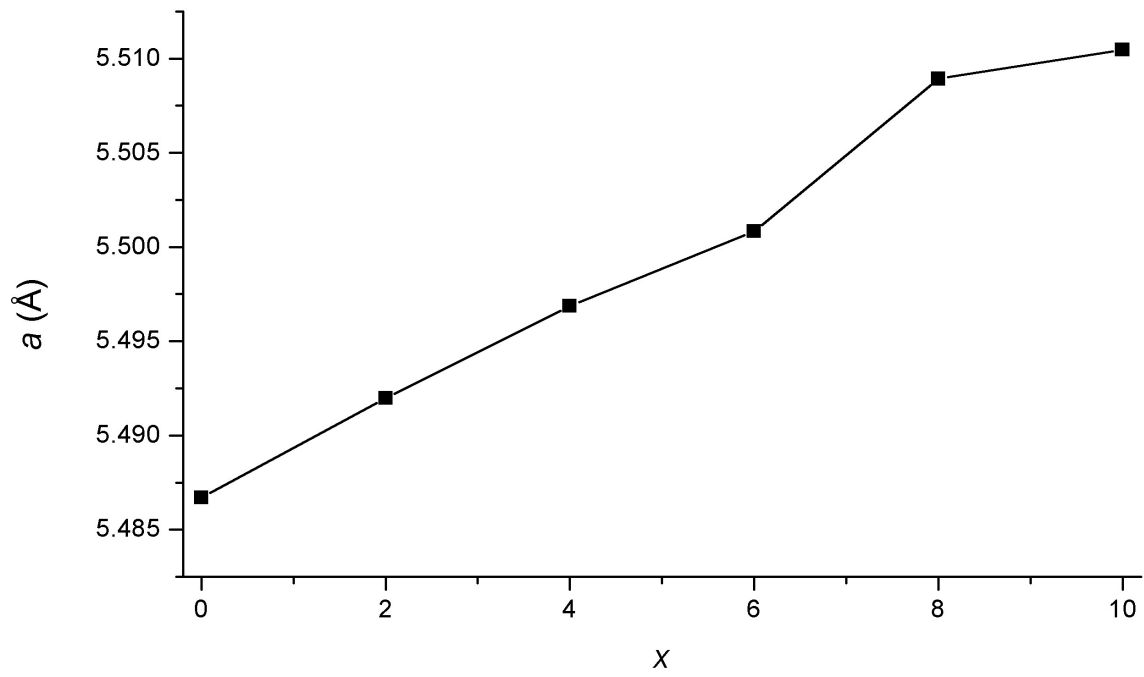


Fig. 3. Compositional variation of the cubic unit cell parameter, a , in samples of composition $\text{Bi}_4\text{Nb}_{1-x}\text{Y}_x\text{O}_{8.5-x}$ quenched from high temperature. Data for the $x = 0.0$ composition are from [23].

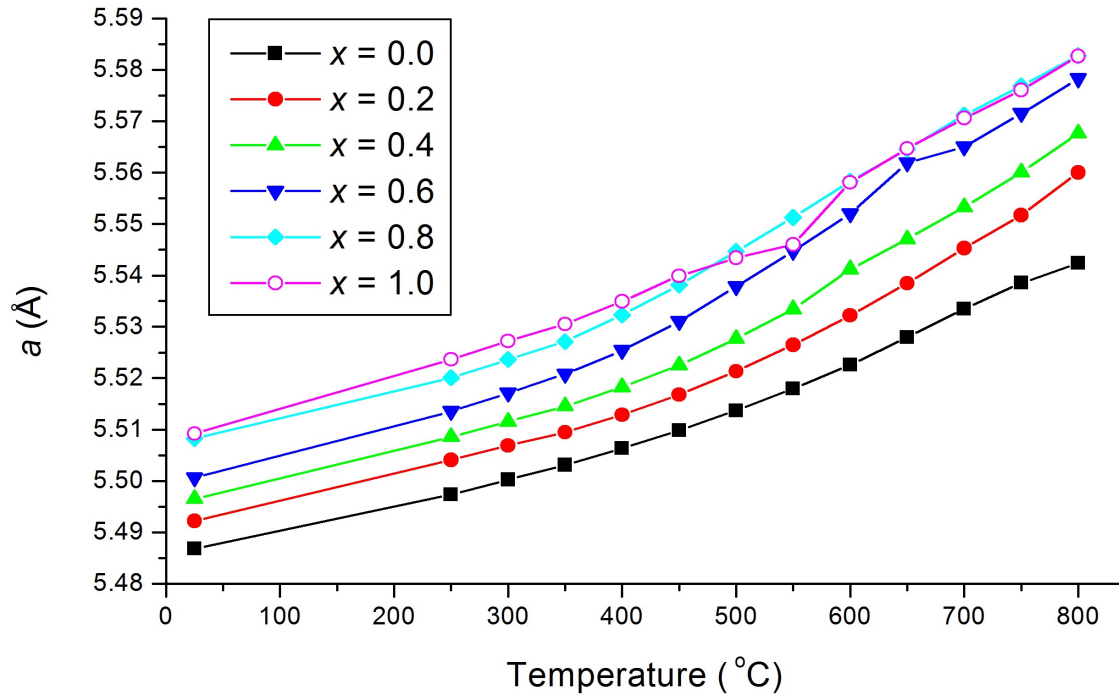


Fig. 4. Thermal variation of the cubic unit cell parameter, a , in samples of composition $\text{Bi}_4\text{Nb}_{1-x}\text{Y}_x\text{O}_{8.5-x}$ quenched from high temperature. Data for the $x = 0.0$ composition are from [23].

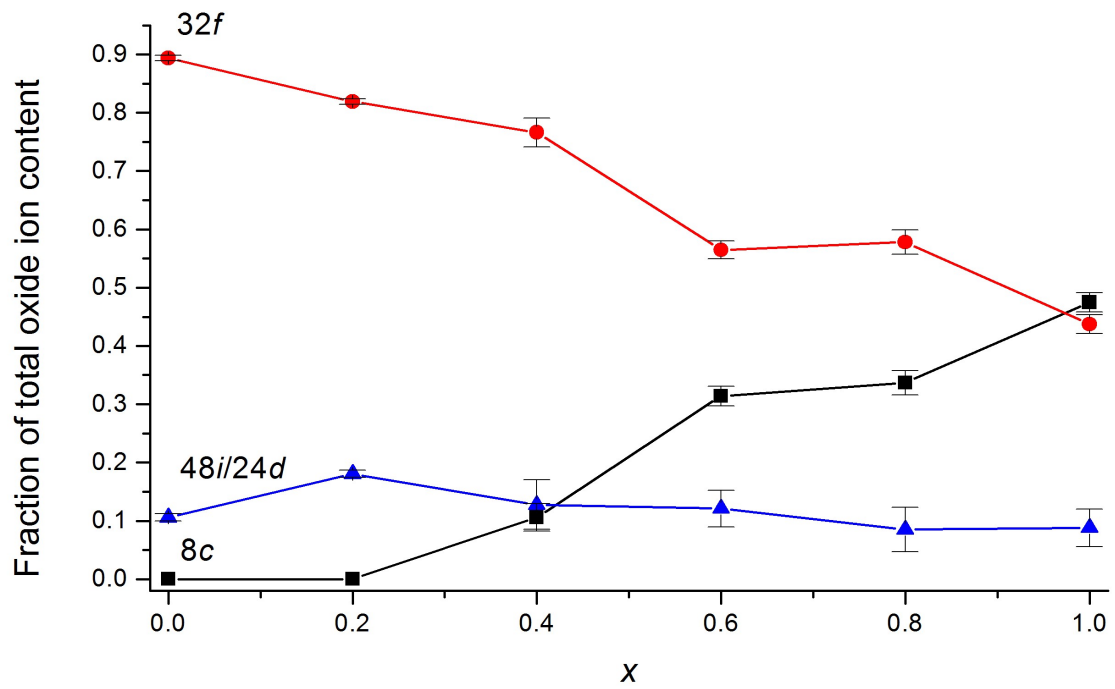


Fig. 5. Compositional variation of oxide-ion site occupancies in samples of $\text{Bi}_4\text{Nb}_{1-x}\text{Y}_x\text{O}_{8.5-x}$ quenched from high temperature. Values are presented as fraction of total oxide-ion content. Data for the $x = 0.0$ composition are from [23].

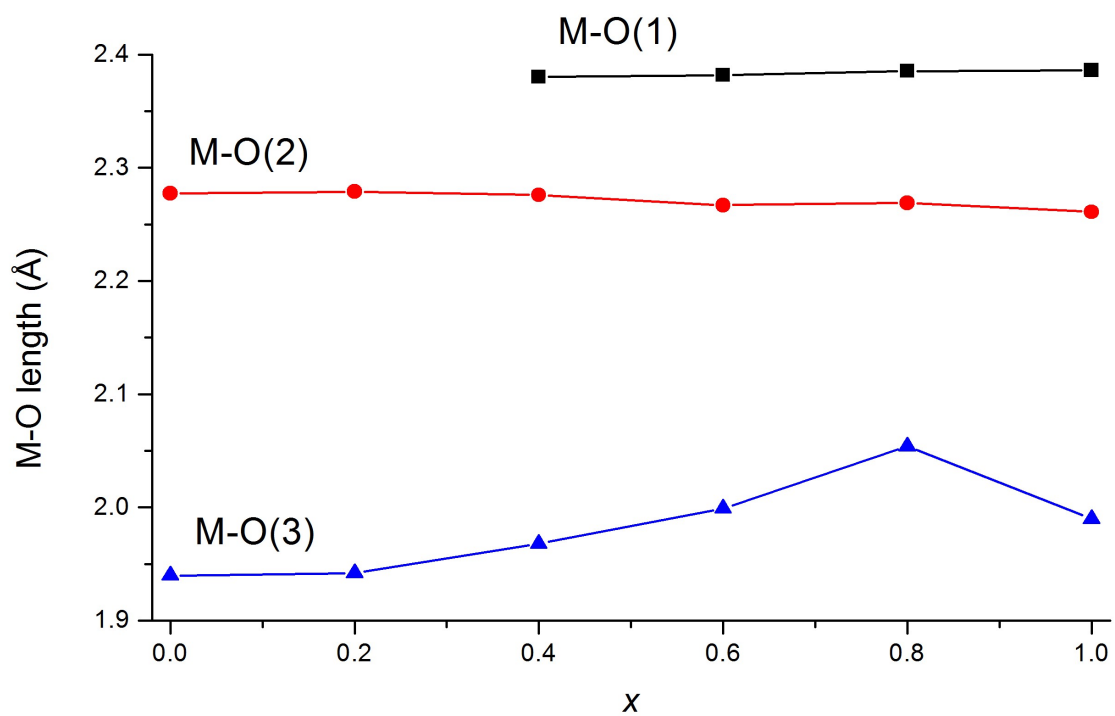


Fig. 6. Compositional variation in M-O bond lengths in samples of $\text{Bi}_4\text{Nb}_{1-x}\text{Y}_x\text{O}_{8.5-x}$ quenched from high temperature. (M = Bi/Nb/Y).

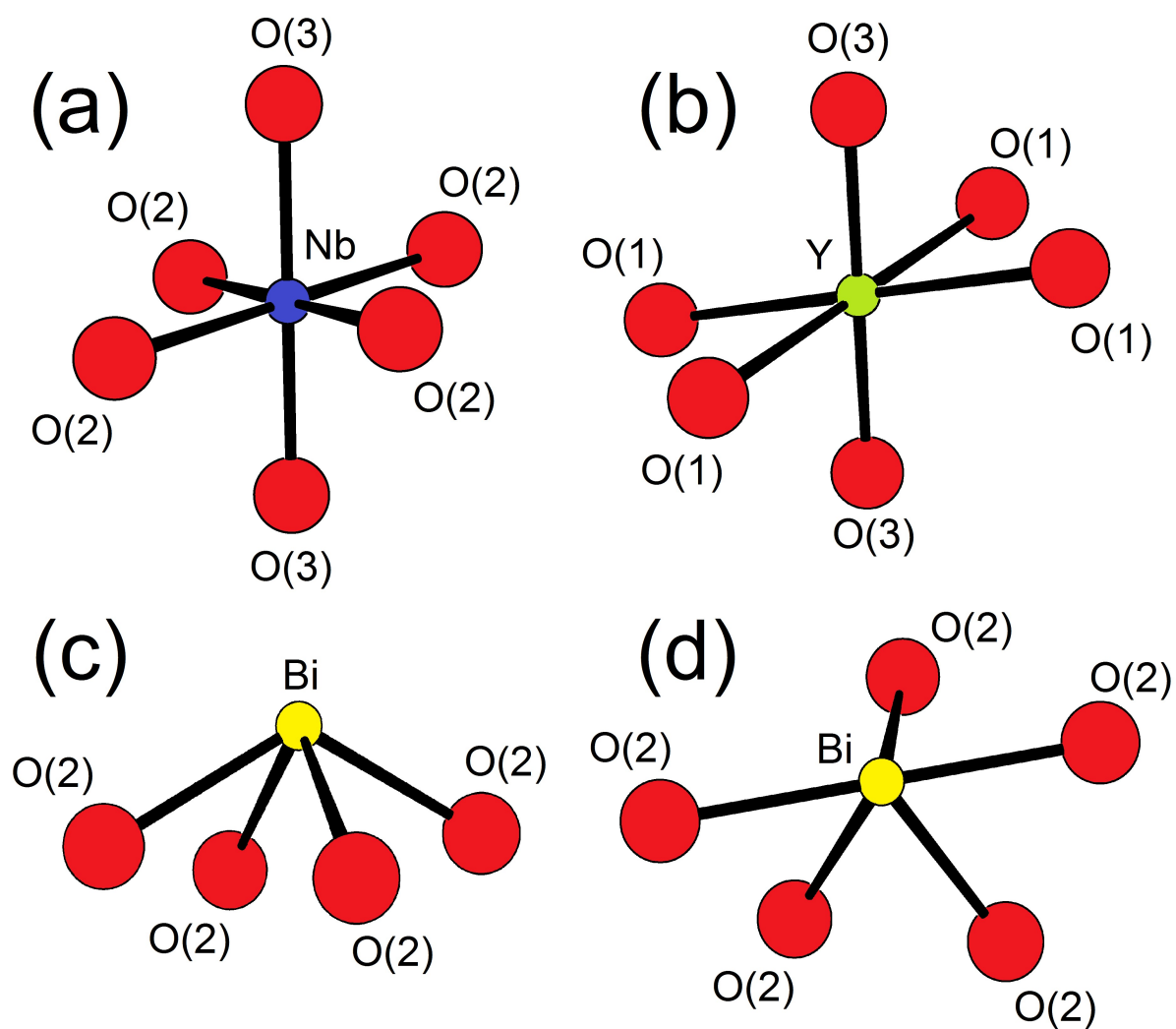
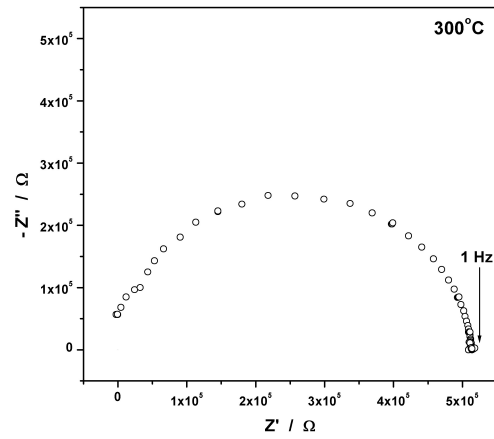
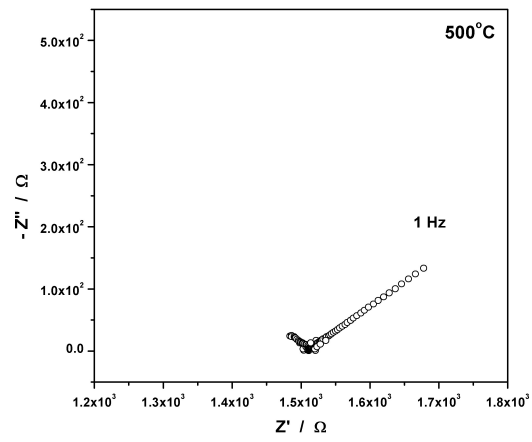


Fig. 7. Proposed coordination geometries for (a) Nb, (b) Y, (c) 4-coordinate Bi and (d) 5-coordinate Bi in quenched samples of $\text{Bi}_4\text{Nb}_{1-x}\text{Y}_x\text{O}_{8.5-x}$. Images were generated from the refined structural parameters for the $x = 0.4$ composition.

(a)



(b)



(c)

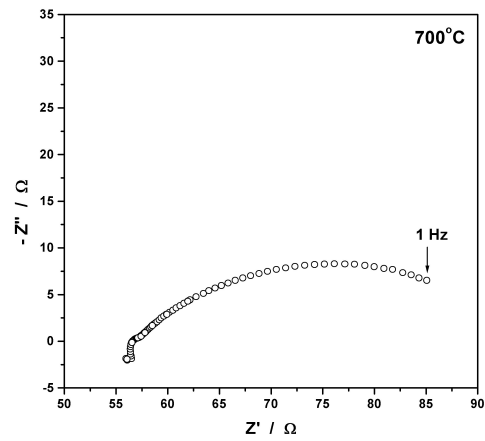


Fig. 8. Representative impedance spectra at (a) 300 °C, (b) 500 °C and (c) 700 °C. Data for the $x = 0.4$ composition are shown.

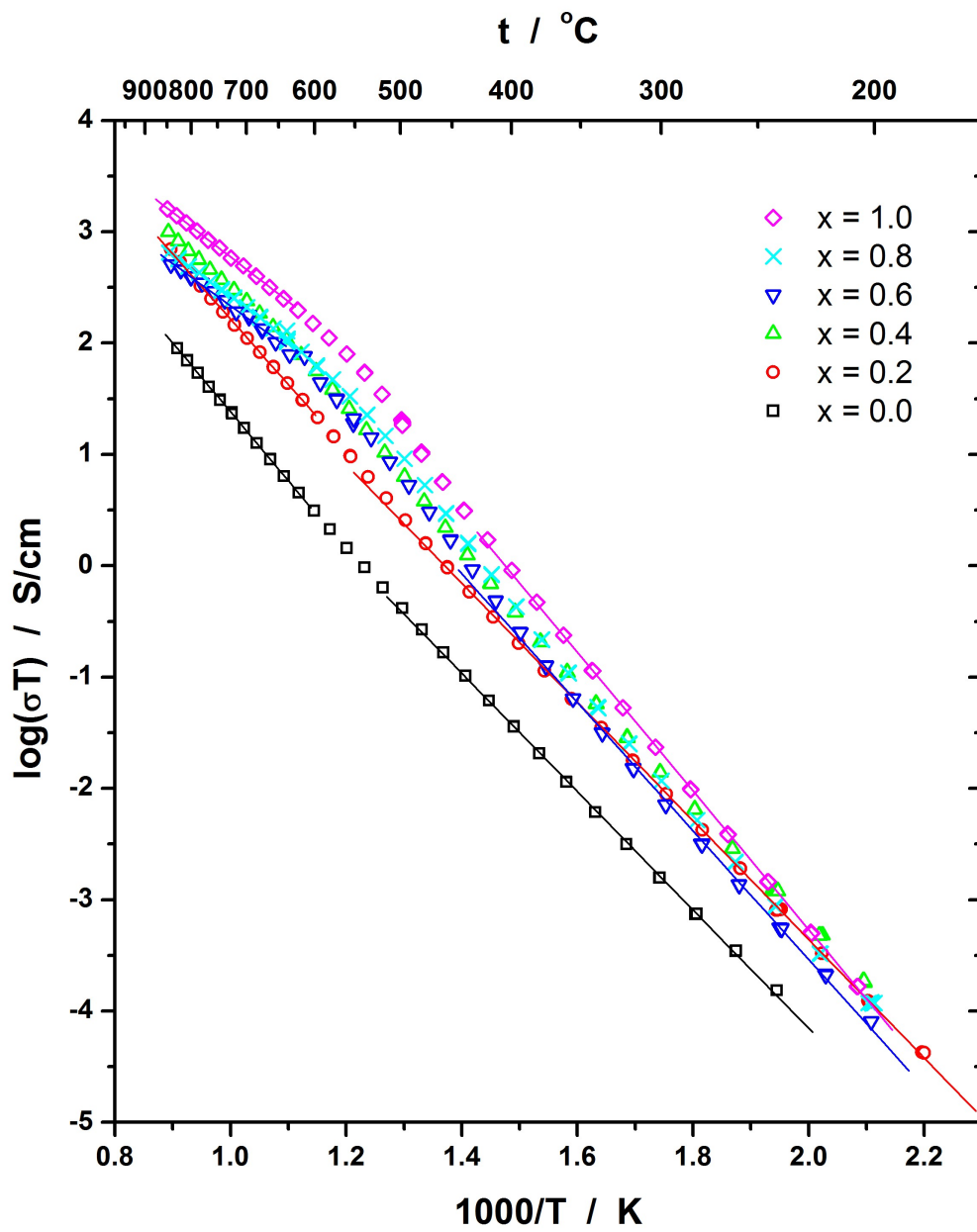


Fig. 9. Arrhenius plots of total conductivity for compositions in the $\text{Bi}_4\text{Nb}_{1-x}\text{Y}_x\text{O}_{8.5-x}$ system. Data for the $x = 0.0$ composition are from [23].

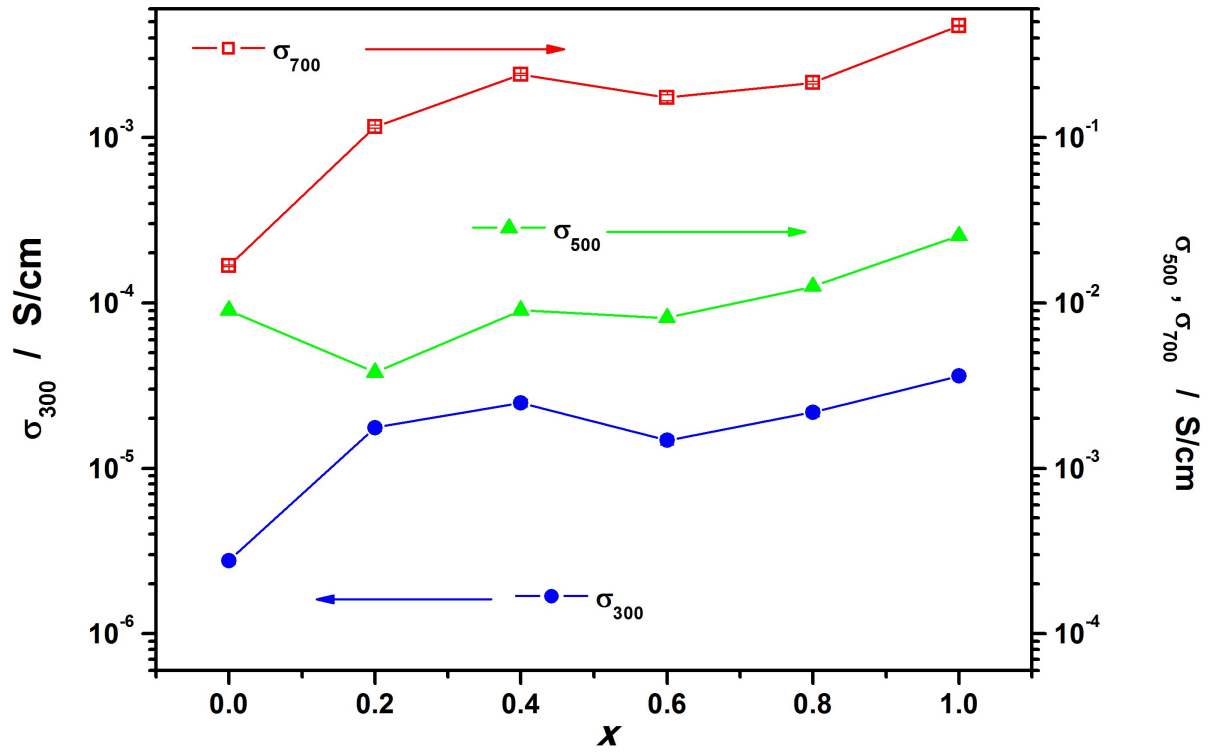


Fig. 10. Compositional variation of low temperature (σ_{300}), intermediate temperature (σ_{500}), and high temperature (σ_{700}) conductivity in the $\text{Bi}_4\text{Nb}_{1-x}\text{Y}_x\text{O}_{8.5-x}$ system. Data for the $x = 0.0$ composition are from [23].

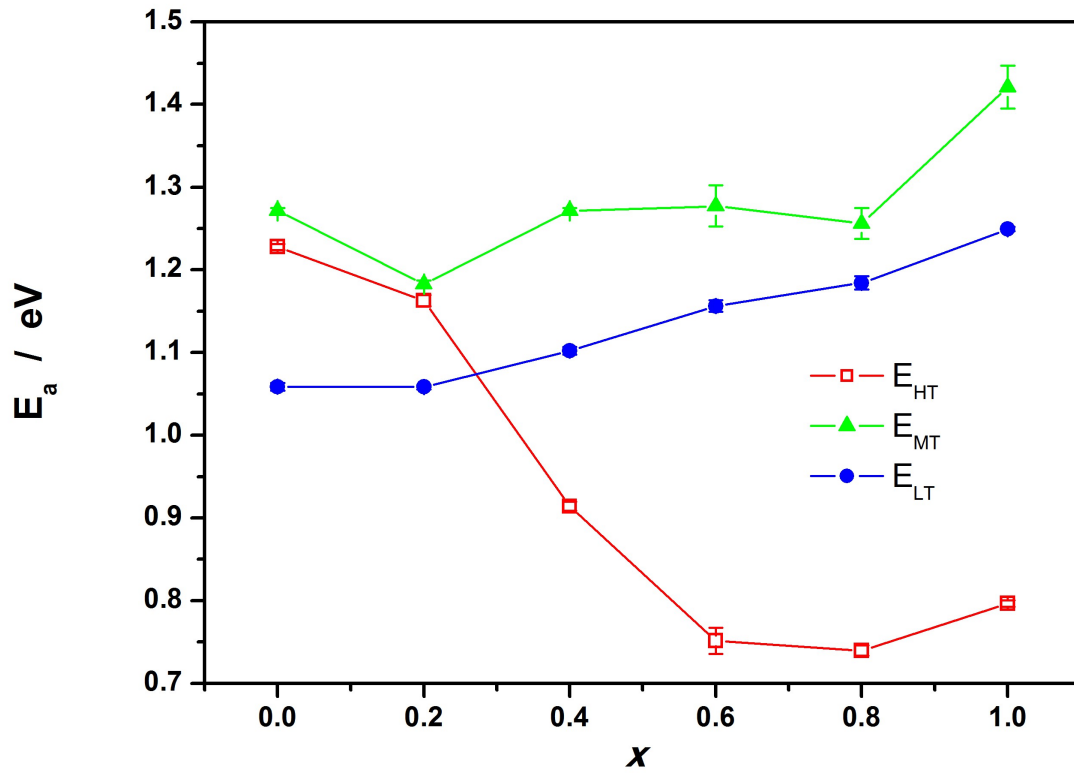


Fig. 11. Compositional variation of low-temperature (ΔE_{LT}), intermediate-temperature (ΔE_{MT}) and high-temperature (ΔE_{HT}) activation energies. Data for the $x = 0.0$ composition are from [23].